The Adaptive Lagrangian Particle Method for Macroscopic and Micro-Macro Computations of Time-Dependent Viscoelastic Flows

X. Gallez, P. Halin, G. Lielens, R. Keunings, V. Legat
CESAME, Division of Applied Mechanics, Université catholique de Louvain, B-1348 Louvain-la-Neuve, Belgium

Abstract

We propose a new numerical technique, referred to as the Adaptive Lagrangian Particle Method (ALPM), for computing time-dependent viscoelastic flows using either a differential constitutive equation (macroscopic approach) or a kinetic theory model (micro-macro approach). In ALPM, the Eulerian finite element solution of the conservation equations is decoupled from the Lagrangian computation of the extra-stress at a number of discrete particles convected by the flow. In the macroscopic approach, the extra-stress carried by the particles is obtained by integrating the constitutive equation along the particle trajectories. In the micro-macro approach, the extra-stress is computed by solving along the particle paths the stochastic differential equation associated to the kinetic theory model. At each time step, ALPM automatically enforces that all elements of the mesh have a number of Lagrangian particles ranging within a user-specified interval. Results are given for the start-up flow between highly eccentric rotating cylinders, using the FENE and FENE-P dumbbell models for dilute polymer solutions.

1 Introduction

The development of numerical methods for solving complex viscoelastic flow problems has been the subject of active research efforts over the last 20 years. A vivid historical account is found in the book by Tanner and Walters [1]. Until recently, viscoelastic flow simulations have been based on a purely *macroscopic* approach that couples the numerical solution of the conservation laws with the integration of a suitable rheological constitutive equation. Progress in macroscopic viscoelastic flow computations has been impressive indeed (see e.g. the review literature [2-6]), to the extent that

much of the focus has now shifted towards modeling issues such as the evaluation of constitutive equations in complex flows. The subject is by no means closed, however. In particular, robust and efficient techniques remain to be developed for addressing the complex three-dimensional and time-dependent problems relevant to laboratory or industrial applications.

A novel paradigm for viscoelastic flow simulations was introduced in 1992 by Öttinger and Laso [7, 8], under the now famous acronym CONNFFESSIT (Calculation Of Non-Newtonian Flows: Finite Elements and Stochastic SImulation Technique). It is basically a *micro-macro* approach that combines the solution of the conservation equations (macro) with the direct use of a kinetic theory model (micro) describing the rheology of the viscoelastic fluid. Thus, instead of relying on a constitutive equation, one determines the viscoelastic contribution to the stress by means of a coarse-grain model of the molecular dynamics of the fluid. This is achieved using appropriate stochastic simulation techniques. Recent developments in the emerging micro-macro approach to viscoelastic flow computations are reported in [9-14].

Micro-macro computations are much more demanding in computer resources than their macroscopic counterparts. They do provide, however, a direct link between the flow-induced development of the micro-structure (e.g. molecular orientation and stretch) and the flow operating conditions. Also, micro-macro simulations can be used to guide the development of improved constitutive equations. These points have been substantiated in recent studies of dilute polymer solutions. In this particular framework, a useful kinetic theory model describes the fluid as a suspension of dumbbells convected in a Newtonian solvent [15]. The dumbbell model consists of two Brownian beads connected by a spring. It describes in a coarse-grain manner the intramolecular interactions taking place in the polymer (through the spring force), as well as the polymer-solvent interactions (through Stokes drag and Brownian forces acting on the beads). The polymer configuration state is thus described by the orientation and length of the vector $\boldsymbol{Q}$ connecting the two beads. Interestingly, if one assumes that the connector force is linear in $\boldsymbol{Q}$, the kinetic theory can be exploited fully and without mathematical approximations to yield an equivalent constitutive equation known as the Oldroyd-B model. This particular constitutive equation is a realistic model of dilute polymer solutions in flows that do not extend the polymer molecules close to their maximum extension (i.e. their contour length) (e.g. [16-19]). In modeling stronger flows, finite extensibility of the polymer must be taken into account. One approach is the Finitely Extensible Non-Linear Elastic

(FENE) dumbbell model, which makes use of a connector force that is a non-linear function of $\boldsymbol{Q}$. The force is singular at maximum extension, thus preventing the dumbbell from extending beyond a specified length. Recent stochastic simulations of FENE dumbbells have demonstrated the value of this non-linear and yet rather crude kinetic theory model (e.g. [20-22]). The important point here is that the FENE model cannot be translated into a mathematically equivalent constitutive equation. The so-called FENE-P constitutive equation [15] can be derived from the FENE theory using a mathematical (closure) approximation due to Peterlin. As shown in [21, 23, 24], the impact of the closure approximation is significant; in other words, the FENE and FENE-P rheological properties differ markedly in certain flows. Stochastic simulations of FENE dumbbells have been exploited recently [21] to derive improved closure approximations of the kinetic theory. The need remains, however, for micro-macro simulation techniques that make direct use of a kinetic theory model, without relying on closure approximations of questionable value.

In a recent paper [14], we have proposed a new numerical technique, referred to as the Lagrangian Particle Method (LPM), for solving time-dependent viscoelastic flows using either the macroscopic or the micro-macro approach. Briefly, LPM decouples at each time step the Eulerian finite element solution of the conservation equations and the Lagrangian computation of the polymer stress. A specified number of discrete particles is convected by the flow, and the polymer stress carried by the particles is obtained by integrating along the particle paths either the constitutive equation (macroscopic approach), or the stochastic differential equation (micro-macro approach). In [14], LPM was used successfully for computing the start-up flow of a dilute polymer solution between *slightly* eccentric rotating cylinders, using the FENE-P (macroscopic) and FENE (micro-macro) dumbbell models.

As stated in [14], a major next step in the further development of LPM is the design of an *adaptive* algorithm that would allow the automatic creation or deletion of Lagrangian particles when and where needed. In the present paper, we propose a first version of the Adaptive Lagrangian Particle Method (ALPM), wherein the number of Lagrangian particles in each element of the mesh is automatically kept within a user-specified interval during the course of the simulation. ALPM is evaluated in the start-up flow of FENE-P and FENE fluids between *highly* eccentric rotating cylinders, which indeed is a much more challenging problem than the small-eccentricity case considered in [14]. The simulation results clearly demonstrate the value of the adaptive

algorithm.

The paper is organized as follows. In Section 2, we detail the equations governing the flow of FENE and FENE-P fluids. Section 3 gives an overview of the basic technical features of LPM. The large-eccentricity LPM simulation results are reported and discussed in Section 4. We describe in Section 5 the basic adaptive algorithm of ALPM, and report the ALPM simulation results in Section 6. Finally, we conclude in Section 7.

2 Governing equations

In the present paper, we consider the time-dependent isothermal flow of an incompressible viscoelastic fluid in a two-dimensional confined geometry Ω with boundary $\partial\Omega$. The Eulerian formulation of the conservation laws for linear momentum and mass read [25]

$$\rho \, \frac{D\boldsymbol{v}}{Dt} = \boldsymbol{\nabla} \cdot \left(-p \, \boldsymbol{I} + \boldsymbol{\tau} \right), \tag{1}$$

$$\boldsymbol{\nabla} \cdot \boldsymbol{v} = 0. \tag{2}$$

Here, ρ is the density, p and $\boldsymbol{v}$ are the pressure and velocity fields, respectively, $\boldsymbol{I}$ is the unit tensor, $\frac{D\cdot}{Dt}$ is the material time derivative operator, and $\boldsymbol{\tau}$ is the extra-stress tensor. We have neglected body forces in the momentum equation. The conservation laws (1-2) must be closed with a suitable model relating the deformation history of the fluid to the extra-stress tensor $\boldsymbol{\tau}$. In computational studies, it is usual to write the extra-stress $\boldsymbol{\tau}$ as the sum of a purely-viscous Newtonian contribution $\boldsymbol{\tau}_N$ and a polymer contribution $\boldsymbol{\tau}_p$,

$$\boldsymbol{\tau} = \boldsymbol{\tau}_N + \boldsymbol{\tau}_p, \qquad \boldsymbol{\tau}_N = 2\eta_N \boldsymbol{D}, \tag{3}$$

where $\boldsymbol{D}$ is the rate of deformation tensor $\frac{1}{2}\left(\boldsymbol{\nabla v} + \boldsymbol{\nabla v}^T\right)$ and η_N is a constant shear viscosity coefficient. In the context of polymer melts, $\boldsymbol{\tau}_N$ accounts for the fast relaxation modes. For polymer solutions, $\boldsymbol{\tau}_N$ is the solvent contribution to the extra-stress. The polymer extra-stress $\boldsymbol{\tau}_p$ is itself often written as the finite sum of individual contributions $\boldsymbol{\tau}_p^{(i)}$, each corresponding to one data of the discrete linear relaxation spectrum,

$$\boldsymbol{\tau}_p = \sum_{i=1}^{N_{sp}} \boldsymbol{\tau}_p^{(i)}. \tag{4}$$

Non-linear coupling between the modes is neglected in this formulation. The numerical techniques presented in this paper are applied to the case of a single relaxation time ($N_{sp} = 1$); they can readily be extended to a finite spectrum ($N_{sp} > 1$).

We shall consider two approaches for determining the polymer stress $\boldsymbol{\tau}_p$: a macroscopic constitutive equation of the differential type, and a coarse-grain kinetic theory model of the polymer dynamics. The generic form of differential constitutive equations used in computational rheology reads

$$\frac{D\boldsymbol{\tau}_p}{Dt} = \boldsymbol{f}(\boldsymbol{\tau}_p, \boldsymbol{\kappa}), \tag{5}$$

where $\boldsymbol{\kappa}$ is the velocity gradient and $\boldsymbol{f}$ is a model-dependent tensor function of $\boldsymbol{\tau}_p$ and $\boldsymbol{\kappa}$. Equation (5) governs the evolution of the polymer stress along each particle path of the memory fluid. The class of kinetic theory models [15] considered in this paper describes the molecular configurations of the polymer molecules by means of suitable geometrical quantities denoted globally by $\boldsymbol{X}$. A diffusion equation is derived that governs the evolution of the probability distribution function $\psi(\boldsymbol{X}, t)$ for the configurations at each material point of the continuum. The polymer stress $\boldsymbol{\tau}_p$ is then obtained at each material point by means of suitable averages over the configuration space.

For the sake of illustration, we consider below the kinetic theory of dilute polymer solutions known as the Warner **F**initely **E**xtensible **N**on-Linear **E**lastic (FENE) dumbbell model [15]. The polymer solution is viewed as a flowing suspension of dumbbells that are convected by the Newtonian solvent and that do not interact with each other. Each dumbbell consists of two identical Brownian beads connected by a spring. In this coarse-grain picture, the beads are the interaction sites with the solvent (slow viscous drag and thermal Brownian forces), while the connector spring force models intramolecular interactions. So, the configuration state $\boldsymbol{X}$ is simply given by the vector $\boldsymbol{Q}$ connecting the two beads of each dumbbell. In the FENE theory, the spring force $\boldsymbol{F}^c$ is defined as

$$\boldsymbol{F}^c(\boldsymbol{Q}) = \frac{H}{1 - \boldsymbol{Q}^2/Q_0^2}\,\boldsymbol{Q}\ , \tag{6}$$

where H is a spring constant and Q_0 is the maximum dumbbell length beyond which the polymer cannot be extended. The diffusion equation that governs the evolution of the configuration distribution function $\psi(\boldsymbol{Q}, t)$ reads for non-

homogeneous flows as follows [15]

$$\frac{\partial \psi}{\partial t} + \boldsymbol{v} \cdot \frac{\partial \psi}{\partial \boldsymbol{x}} = -\frac{\partial}{\partial \boldsymbol{Q}} \cdot \left[\left\{ \boldsymbol{\kappa} \cdot \boldsymbol{Q} - \frac{2}{\zeta} \, \boldsymbol{F}^c(\boldsymbol{Q}) \right\} \psi \right] + \frac{2kT}{\zeta} \, \frac{\partial}{\partial \boldsymbol{Q}} \cdot \frac{\partial}{\partial \boldsymbol{Q}} \, \psi, \quad (7)$$

where ζ is the friction coefficient of the beads, T is the absolute temperature, k is the Boltzmann constant, and $\boldsymbol{x}$ denotes the spatial position. Assuming that $\psi(\boldsymbol{Q}, t)$ is known at each material point, the polymer stress $\boldsymbol{\tau}_p$ is then obtained by means of Kramers' expression [15]

$$\boldsymbol{\tau}_p = -nkT\boldsymbol{I} + n \, \langle \boldsymbol{Q}\boldsymbol{F}^c(\boldsymbol{Q}) \rangle, \quad (8)$$

where n is the dumbbell number density and the angular brackets $\langle \cdot \rangle$ denote the configuration space average $\int \cdot \, \psi \, d\boldsymbol{Q}$. A convenient way of exploiting Kramers' expression (8) consists in integrating along the flow trajectories the Itô stochastic differential equation [26]:

$$d\boldsymbol{Q} = [\boldsymbol{\kappa} \cdot \boldsymbol{Q} - \frac{2}{\zeta} \boldsymbol{F}^c(\boldsymbol{Q})] \, dt + \sqrt{\frac{4kT}{\zeta}} \, d\boldsymbol{W}, \quad (9)$$

where $\boldsymbol{W}$ is the three-dimensional Wiener process, namely a Gaussian stochastic process with vanishing mean and covariance $\langle \boldsymbol{W}(t_1) \, \boldsymbol{W}(t_2) \rangle = min(t_1, t_2) \, \boldsymbol{I}$. Indeed, Eq. (9) is an evolution equation for the Markovian process $\boldsymbol{Q}$ whose probability density ψ is solution of the diffusion equation (7). Thus, equations (9) et (7) are mathematically equivalent. In the stochastic simulation approach, one numerically computes the evolution of many realizations of the stochastic process $\boldsymbol{Q}$ (via Eq. (9)); the polymer stress $\boldsymbol{\tau}_p$ is then obtained by means of Kramers' expression (8), with the configuration average $\langle \cdot \rangle$ replaced by an ensemble average.

The particular differential constitutive equation used in this paper, known as the FENE-P model, is derived from the FENE kinetic theory using a suitable closure approximation due to Peterlin; the FENE spring force (6) is replaced by the self-consistent pre-averaged approximation

$$\boldsymbol{F}^c(\boldsymbol{Q}) = \frac{H}{1 - \langle \boldsymbol{Q}^2 \rangle / Q_0^2} \, \boldsymbol{Q}. \quad (10)$$

The Peterlin approximation yields an evolution equation [15] for the configuration tensor $\boldsymbol{A} = \langle \boldsymbol{Q}\boldsymbol{Q} \rangle$:

$$\frac{\partial \boldsymbol{A}}{\partial t} + \boldsymbol{v} \cdot \boldsymbol{\nabla} \boldsymbol{A} - \boldsymbol{\kappa} \cdot \boldsymbol{A} - \boldsymbol{A} \cdot \boldsymbol{\kappa}^T = \frac{4kT}{\zeta} \, \boldsymbol{I} - \frac{4H/\zeta}{1 - tr(\boldsymbol{A})/Q_0^2} \, \boldsymbol{A}, \quad (11)$$

while Kramers' expression (8) and the pre-averaged force law (10) give the FENE-P polymer stress as an algebraic expression of the configuration tensor:

$$\boldsymbol{\tau}_p = -nkT\boldsymbol{I} + n\,\frac{H}{1 - tr(\boldsymbol{A})/Q_0^2}\,\boldsymbol{A}. \tag{12}$$

Equations (11-12) are readily manipulated to yield a differential constitutive equation for $\boldsymbol{\tau}_p$ of the generic form (5). In numerical work, however, it is more convenient to solve the configuration equation (11), which has the same generic form

$$\frac{D\boldsymbol{A}}{Dt} = \boldsymbol{g}(\boldsymbol{A}, \boldsymbol{\kappa}), \tag{13}$$

and then compute $\boldsymbol{\tau}_p$ using Kramers' expression (12). For further reference, we note that the FENE and FENE-P models involve a time constant $\lambda = \zeta/4H$ and a dimensionless finite extensibility parameter $b = HQ_0^2/kT$. The polymer contribution to the zero shear rate viscosity is $\eta_p^0 = nkT\lambda\left(\frac{b}{b+3}\right)$ for the FENE-P fluid, and $\eta_p^0 = nkT\lambda\left(\frac{b}{b+5}\right)$ for the FENE theory.

3 The Lagrangian Particle Method

The Lagrangian Particle Method (LPM) has been described in detail in our recent paper [14]. A typical time step is depicted schematically in Fig. 1.

The Eulerian solution of the conservation equations (1-2) is decoupled at each time step from the Lagrangian computation of the polymer stress along individual particle paths. Let us consider a typical time step $[t_n, t_{n+1} = t_n + \Delta t_{\text{cons}}]$. Using the current polymer stress values $\boldsymbol{\tau}_p(t_n)$ computed in each element at the previous time step, a standard Galerkin finite element technique is applied to the conservation equations to yield the updated velocity and pressure fields at time t_{n+1}. The Galerkin equations read (e.g. [4])

$$\int_\Omega \psi_i \left[\rho\,\frac{D\boldsymbol{v}^a}{Dt}\right]\,d\Omega + \int_\Omega \boldsymbol{\nabla}\psi_i^T \cdot \left[-p^a\boldsymbol{I} + 2\eta_N\boldsymbol{D}^a + \boldsymbol{\tau}_p\right]\,d\Omega = \int_{\partial\Omega} \psi_i\;\boldsymbol{t}\,ds, \tag{14}$$

$$\int_\Omega \pi_j\left[\boldsymbol{\nabla}\cdot\boldsymbol{v}^a\right]\,d\Omega = 0, \tag{15}$$

where ψ_i and π_j are given finite element basis functions for the velocity and pressure respectively ($1 \le i \le N_v, 1 \le j \le N_p$), $\boldsymbol{t}$ is the contact force and

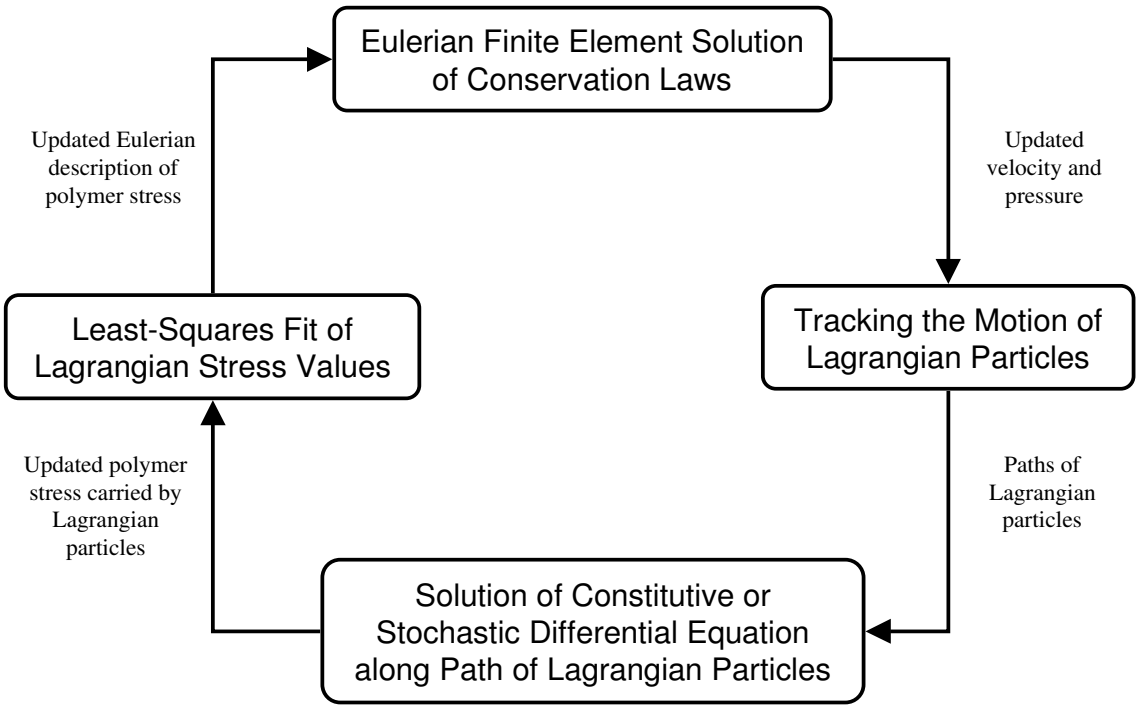

Figure 1: Schematic of the Lagrangian Particle Method (LPM).

s is the arc length measured along the boundary $\partial\Omega$ of the computational domain. In Eqs (14-15), every term marked with the superscript a denotes the corresponding approximation obtained from the finite element expansions

$$\boldsymbol{v}^a(\boldsymbol{x},t) = \sum_{i=1}^{N_v} \boldsymbol{v}^i(t)\ \psi_i(\boldsymbol{x}), \qquad\qquad p^a(\boldsymbol{x},t) = \sum_{j=1}^{N_p} p^j(t)\ \pi_j(\boldsymbol{x}). \tag{16}$$

The Galerkin equations (14-15) constitute a set of first-order differential equations for the unknown nodal values $\boldsymbol{v}^i(t)$ and $p^i(t)$. In LPM, we consider the polymer contribution to (14), namely

$$\int_\Omega \boldsymbol{\nabla}\psi_i^T \cdot \boldsymbol{\tau}_p\ d\Omega, \tag{17}$$

as a known pseudo-body force term evaluated at time t_n. We discretize (14-15) in time using the Euler forward/Euler backward predictor-corrector scheme with a fixed time step $\Delta t_{\rm cons}$. In the current implementation of LPM, a Newton scheme is used to solve the non-linear corrector equations, the initial guess being provided by the predictor. Biquadratic continuous and bilinear continuous basis functions are used for velocity and pressure, respectively.

The new velocity field at time t_{n+1} is then used to update the polymer stress $\boldsymbol{\tau}_p$. In LPM, we compute the polymer stress at a number $N_{\rm part}$ of Lagrangian particles that are convected by the flow, by solving along the computed particle paths either the macroscopic constitutive equation (13) or the stochastic differential equation (9) for a large number of dumbbells carried by each particle. Over the time step $[t_n, t_{n+1}]$, the trajectory $\boldsymbol{r}(t)$ of each Lagrangian particle is determined using the Eulerian velocity field obtained at time t_n; one solves

$$\frac{d\boldsymbol{r}}{dt} = \boldsymbol{v}^a(\boldsymbol{r}, t_n), \tag{18}$$

by means of an element-by-element fourth-order Runge-Kutta method, with a constant time step $\Delta t_{\rm track} \leq \Delta t_{\rm cons}$, and the initial condition $\boldsymbol{r}(t_n)$ known from the previous time step.

Having thus computed the trajectory $\mathcal{T} = \{\boldsymbol{r}(t), t \in [t_n, t_{n+1}]\}$ of each Lagrangian particle, we update the polymer stress as follows. For the FENE-P model, we solve along $\mathcal{T}$ the configuration equation

$$\frac{D\boldsymbol{A}(\boldsymbol{r}(t))}{Dt} = \boldsymbol{g}(\boldsymbol{A}(\boldsymbol{r}(t)), \boldsymbol{\kappa}^a(\boldsymbol{r}(t), t_n)), \tag{19}$$

using a fourth-order Runge-Kutta technique with a constant time step Δt_{const} such that $\Delta t_{\text{track}} \leq \Delta t_{\text{const}} \leq \Delta t_{\text{cons}}$. The initial condition $\boldsymbol{A}(\boldsymbol{r}(t_n))$ is known from the previous time step. For the FENE dumbbell model, each Lagrangian particle carries a number N_d of dumbbells. The configuration $\boldsymbol{Q}$ of each dumbbell is updated by solving along the trajectory $\mathcal{T}$ the stochastic differential equation

$$d\boldsymbol{Q}(\boldsymbol{r}(t)) = [\boldsymbol{\kappa}^a(\boldsymbol{r}(t), t_n) \cdot \boldsymbol{Q}(\boldsymbol{r}(t)) - \frac{2}{\zeta}\boldsymbol{F}^c(\boldsymbol{Q}(\boldsymbol{r}(t)))]dt + \sqrt{\frac{4kT}{\zeta}}\, d\boldsymbol{W}. \quad (20)$$

Again, the initial condition $\boldsymbol{Q}(\boldsymbol{r}(t_n))$ is known from the previous time step. In view of (8), the updated polymer stress carried by a particle is given by the ensemble average

$$\boldsymbol{\tau}_p(\boldsymbol{r}(t_{n+1})) = \frac{n}{N_d} \sum_{i=1}^{N_d} \boldsymbol{Q}^{(i)}(\boldsymbol{r}(t_{n+1}))\ \boldsymbol{F}^c(\boldsymbol{Q}^{(i)}(\boldsymbol{r}(t_{n+1}))) - nkT\ \boldsymbol{I}, \quad (21)$$

where $\boldsymbol{Q}^{(i)}$ is an individual realization of $\boldsymbol{Q}$ ($i = 1, 2, \ldots, N_d$). We solve (20) by means of the Öttinger predictor-corrector scheme [26, 14] of weak order 2 with a constant time step Δt_{stoch} such that $\Delta t_{\text{track}} \leq \Delta t_{\text{stoch}} \leq \Delta t_{\text{cons}}$. We use correlated ensembles of dumbbells [14] in the sense that (i) the same initial ensemble is used in each Lagrangian particle, and (ii) the same N_d independent Wiener processes are generated to compute the configuration of corresponding dumbbells in each particle.

At time t_{n+1}, we thus have at our disposal values of the updated polymer stress $\boldsymbol{\tau}_p$ at discrete Lagrangian particles located at $\boldsymbol{r}^l(t_{n+1})$, for $l = 1, 2, \ldots, N_{\text{part}}$. In order to compute the pseudo-body force integral (17) that will be used to update the velocity field at time $t_{n+2} = t_{n+1} + \Delta t_{\text{cons}}$, we compute in each finite element an Eulerian representation of the polymer stress. This is achieved by computing the bilinear least-squares polynomial that best fits the Lagrangian stress data available in each element at time t_{n+1}. This requires of course that at least four Lagrangian particles be present in each element.

LPM has been used successfully in [14] for solving the start-up flow of FENE and FENE-P fluids in a small-eccentricity journal bearing. In the present paper, we consider the case of a large-eccentricity journal bearing, a much more difficult problem indeed.

4 LPM applied to the large-eccentricity journal bearing problem

We consider the time-dependent, planar flow of FENE and FENE-P fluids between eccentric cylinders, starting from the rest state (Fig. 2). The inner cylinder, of radius R_i, is rotating at a constant angular velocity ω, while the outer cylinder, of radius R_o, is fixed. The axes of the two cylinders are separated by an eccentricity e. We assume that the fluid sticks to the cylinder walls, and specify the rest state as initial conditions. Thus, $\boldsymbol{v}^a(\boldsymbol{x}, t = 0)$ is set to $\mathbf{0}$ over Ω. When using the macroscopic FENE-P constitutive equation, the initial configuration tensor $\boldsymbol{A}$ is set to its equilibrium value identically (this amounts to specifying $\boldsymbol{\tau_p}(\boldsymbol{x}, t = 0) = \mathbf{0}$ over Ω). In the stochastic simulations, the initial dumbbell configurations in each Lagrangian particle are generated using the equilibrium distribution function [15].

The particular flow parameters and material data used in this work are listed in Table 1. The present flow problem is characterized by the dimensionless eccentricity $\epsilon = \frac{e}{R_o - R_i} = 0.67$, the dimensionless gap thickness $\mu = \frac{R_o - R_i}{R_i} = 1.5$, the Reynolds number $Re = \rho\omega R_i(R_o - R_i)/(\eta_N + \eta_p^0) = 0.8$, the Deborah number $De = \lambda\omega R_i/(R_o - R_i) = 1$, the dimensionless finite extensibility $b = 50$, and the viscosity ratio $\beta = \eta_N/(\eta_N + \eta_p^0) = 1/9$.

Flow parameters	$R_i = 1 \quad R_o = 2.5 \quad e = 1.0 \quad \omega = 0.5$
Material data	$\lambda = 3 \quad b = 50 \quad \rho = 1 \quad \eta_N = 0.1 \quad \eta_p^0 = 0.8$

Table 1: Flow parameters and material data used in the simulations (expressed in an arbitrary consistent system of units).

A typical finite element mesh is shown in Fig. 2. We use structured grids with $N_r \times N_\theta$ quadrilateral elements, when N_r and N_θ are the number of uniformly-distributed elements in the radial and azimuthal directions, respectively. The numerical results shown in this section have been obtained with the 10×40 mesh of Fig. 2 with $\Delta t_{\text{cons}} = 10^{-2}$ and $\Delta t_{\text{track}} = \Delta t_{\text{const}} = 10^{-3}$. The numerical solutions will be presented in terms of the temporal evolution of the velocity and polymer stress in the region of narrowest gap (Fig. 2), where the largest velocity and polymer stress gradients develop.

The small-eccentricity problem ($\epsilon = 0.1$) studied in our previous paper [14]

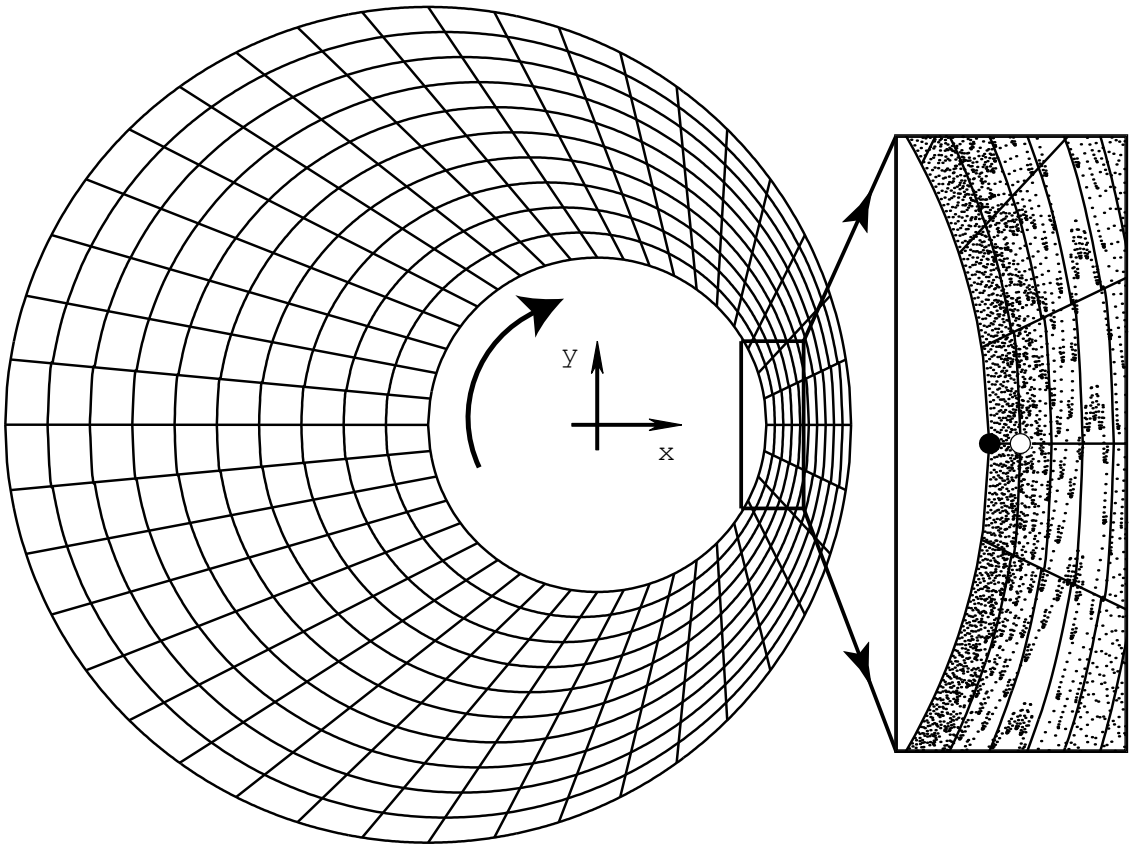

Figure 2: Finite element mesh for computing the start-up flow in a journal bearing. The enlargement shows a number of Lagrangian particles convected by the flow, as well as the locations where the computed polymer stress (•) and velocity (∘) are displayed in subsequent figures.

is essentially a perturbed viscometric flow without recirculation flow lines. The picture is quite different in the large eccentricity case, as shown in Fig. 3. Here, we illustrate the steady-state streamlines computed for the FENE-P fluid. There is a significant recirculation zone in the region of large gap where fluid elements are about 200 times slower than those flowing along the quasi-circular paths induced by the moving cylinder. The converging-diverging flow region located between these two distinct regimes constitutes as we shall see a numerical challenge for LPM.

Figure 4 shows the large-eccentricity results obtained with LPM for the FENE-P fluid. Several simulations are depicted, for a fixed number $N_{\rm part}$ of Lagrangian particles ranging between 3600 and 810000. In each case, the particles are distributed uniformly in each element at time $t = 0$. The LPM results of Fig. 4 are thus for an *average* number of particles per element $N^{\rm elt}_{\rm part}$ between 9 and 2025. While the specification $N^{\rm elt}_{\rm part} = 9$ was used successfully in [14] for solving the corresponding small-eccentricity problem, inspection of Fig. 4 reveals that many more particles are needed in the large-eccentricity case to obtain stable and accurate LPM results. Indeed, the LPM simulations with $N^{\rm elt}_{\rm part} = 9$ and 25 failed before obtaining the steady-state. With $N^{\rm elt}_{\rm part} = 100$, the transient response is computed accurately, but the results become unstable once the steady-state is reached. Use of more particles yields stable and accurate results. In fact, the LPM results obtained with $N^{\rm elt}_{\rm part} = 256$ are quite satisfactory for typical rheological studies. The results obtained with $N^{\rm elt}_{\rm part} = 2025$ have converged numerically at the scale of the drawing; they will be used in the sequel as reference solution.

The LPM simulation with $N^{\rm elt}_{\rm part} = 9$ failed at time $t \sim 2$, where one finite element happens to have less than four particles. It is useful to examine in Fig. 5 how would the spatial and statistical distributions of the particles evolve at later times using the uncoupled (i.e. Newtonian) flow kinematics. Clearly, many elements located in the converging-diverging flow region do not have enough particles; some are even empty.

Similar histograms of the statistical distribution of particles in the elements are shown in Fig. 6 for the LPM simulations with $N^{\rm elt}_{\rm part} = 100$ and 256; the information is given for time $t = 10$, where the steady-state solution is essentially reached. We see that all elements have enough particles, thus producing satisfactory numerical results. The statistical distribution of particles, however, has spread significantly relative to the initial distribution (i.e. a Dirac function located at $N^{\rm elt}_{\rm part}$). This implies that many elements may be richer in particles than actually warranted for numerical stability

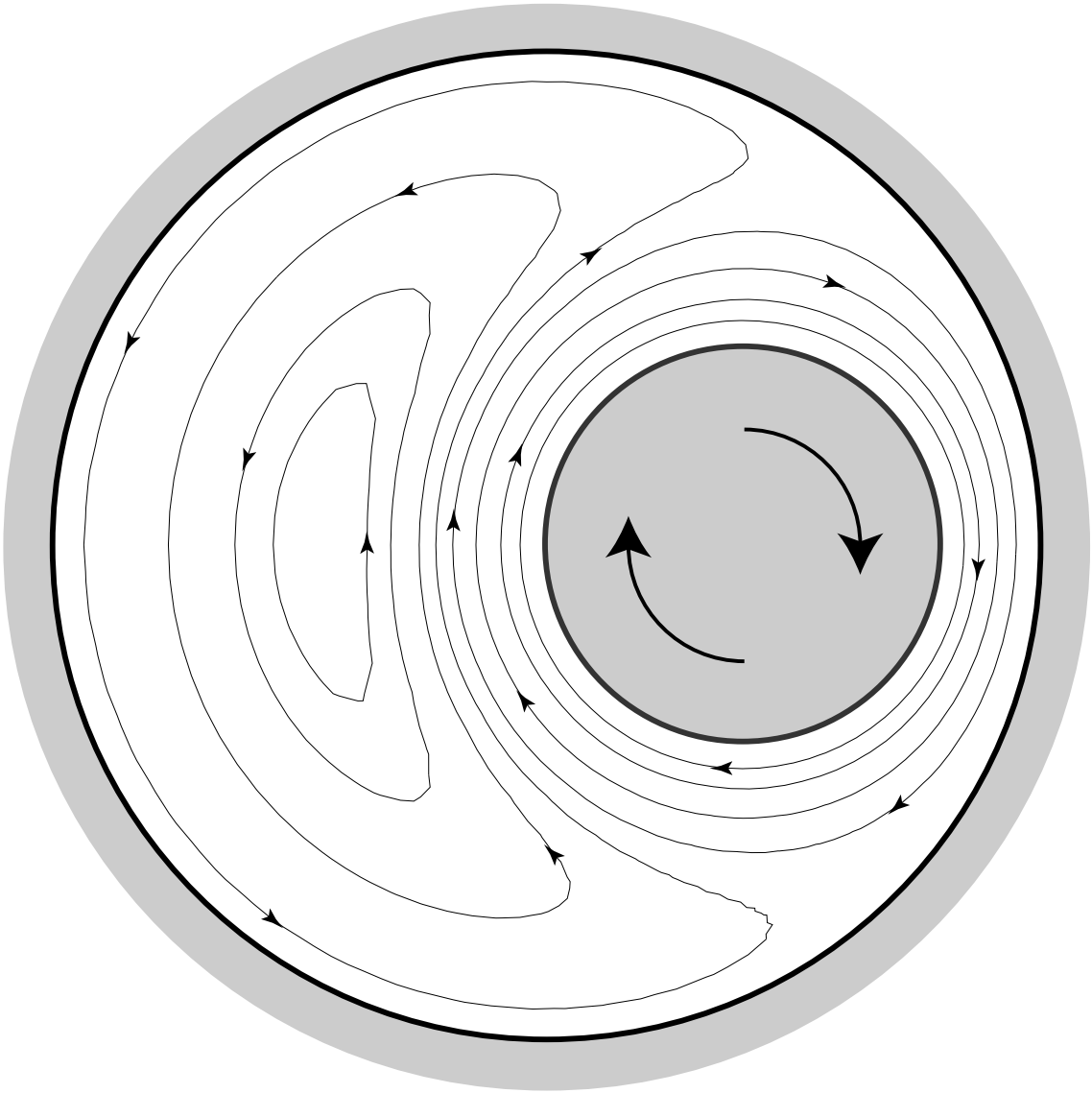

Figure 3: Steady-state streamlines computed with the FENE-P constitutive equation.

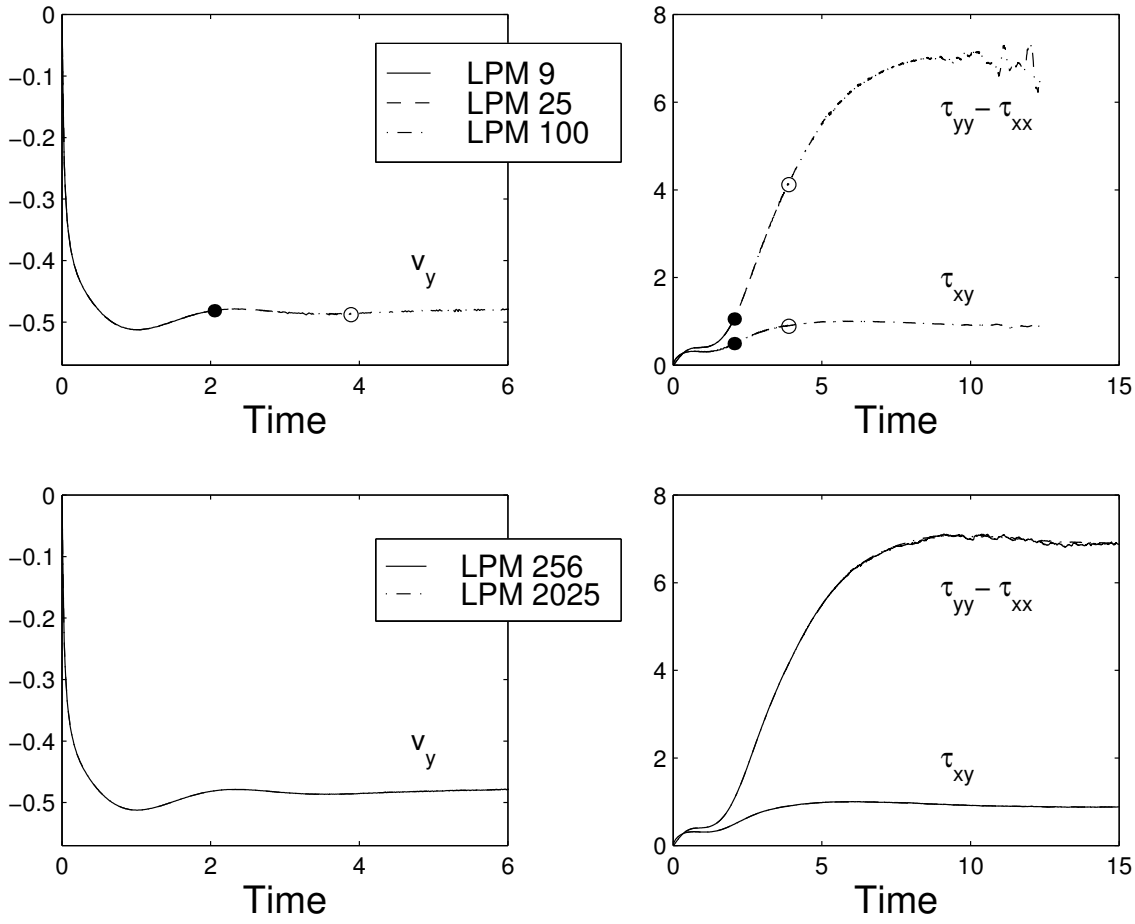

Figure 4: Temporal evolution of velocity and polymer stress in the region of thinnest gap (see Fig. 2) obtained with LPM and the FENE-P constitutive equation. The average number of particles per element $N_{\text{part}}^{\text{elt}}$ ranges between 9 and 2025. With $N_{\text{part}}^{\text{elt}} = 9$, the LPM simulation fails at $t \sim 2$ ($\bullet$). The LPM results with $N_{\text{part}}^{\text{elt}} = 25$ and 100 become numerically unstable near $t = 4$ ($\circ$) and 10 respectively. Numerical convergence is observed for higher values of $N_{\text{part}}^{\text{elt}}$.

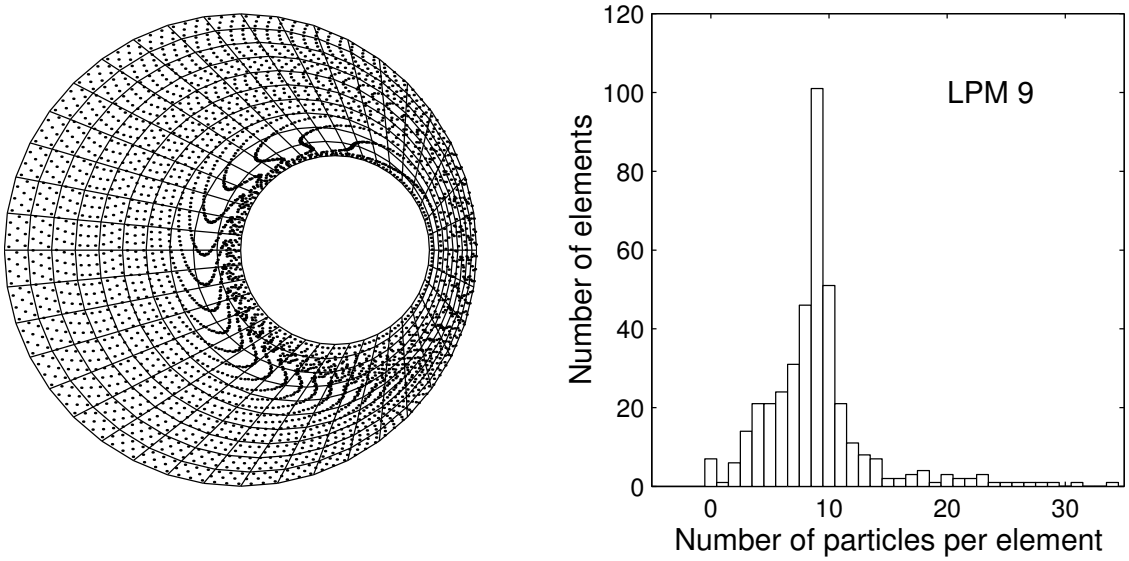

Figure 5: LPM simulation for the FENE-P fluid with an average of $N_{\text{part}}^{\text{elt}} = 9$ particles per element. Spatial and statistical distributions of the particles at time $t = 10$ using uncoupled (i.e. Newtonian) flow kinematics.

and accuracy. There is thus a need for an *adaptive* version of LPM, referred to in the remainder of the paper as ALPM, where the number of Lagrangian particles is allowed to vary during the course of a particular simulation.

5 The Adaptive Lagrangian Particle Method

A typical time step of ALPM is depicted schematically in Fig. 7. ALPM and LPM are essentially equivalent (compare with Fig. 1), the exception being the new adaptivity block. The latter involves three basic steps; namely (i) creation, (ii) initialization, and (iii) destruction of Lagrangian particles. At each time step, ALPM enforces that all elements of the mesh have a number of Lagrangian particles in the user-specified interval $[N_{\text{part}}^{\text{elt,min}}, N_{\text{part}}^{\text{elt,max}}]$. How this is achieved is briefly described next. For more details regarding the computer implementation of ALPM, see [27].

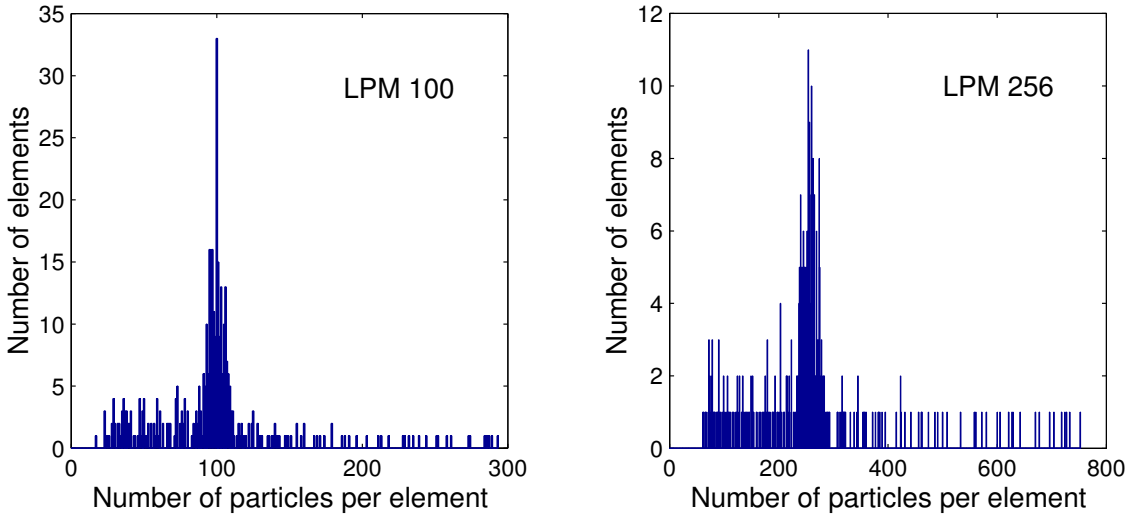

Figure 6: LPM simulations for the FENE-P fluid with an average of $N_{\rm part}^{\rm elt} = 100$ and 256 particles per element. Statistical distribution of the particles at time $t = 10$ (see Fig. 4).

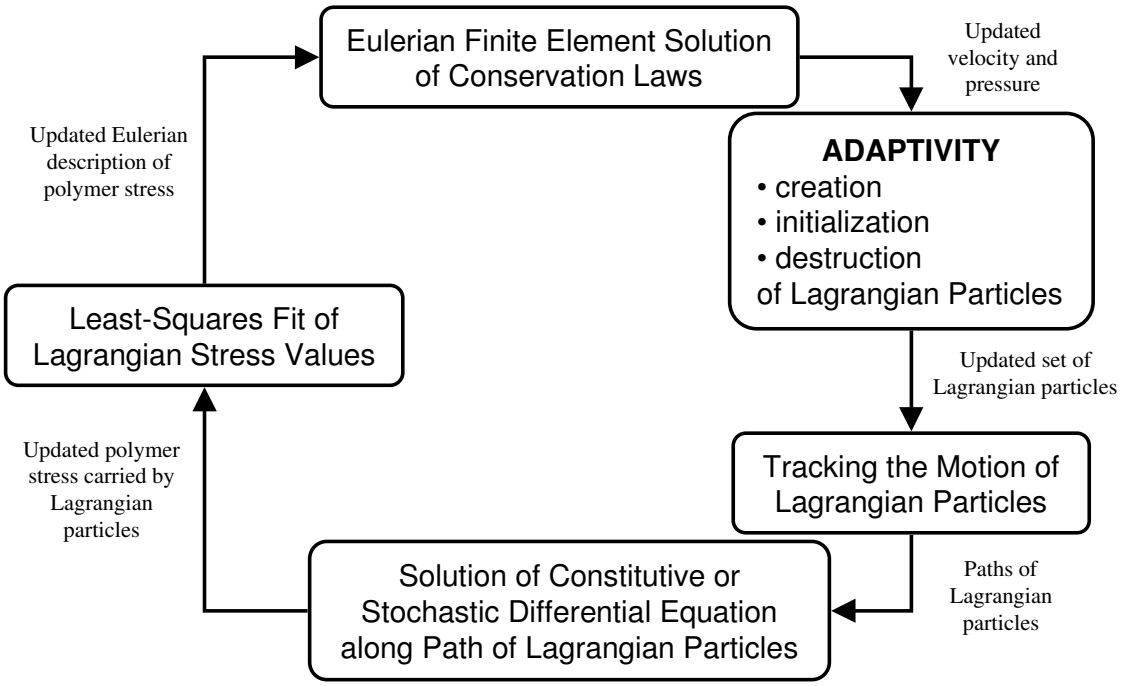

Figure 7: Schematic of the Adaptive Lagrangian Particle Method (ALPM).

5.1 Creation of Lagrangian particles

In each quadrilateral finite element, let us define a uniform grid of $\sqrt{N_{\text{part}}^{\text{elt,min}}} \times \sqrt{N_{\text{part}}^{\text{elt,min}}}$ so-called Reference Locations (RL). As shown in Fig. 8, the RL's are the locations where the specified minimum number of particles would be located if they were distributed uniformly. ALPM then checks that at least one particle of the element is close enough to each RL, i.e. that it is enclosed in a square box centered about the RL. If no particle is found to be close enough to a particular RL, ALPM creates a new particle there. Figure 8 illustrates the creation step for one new Lagrangian particle.

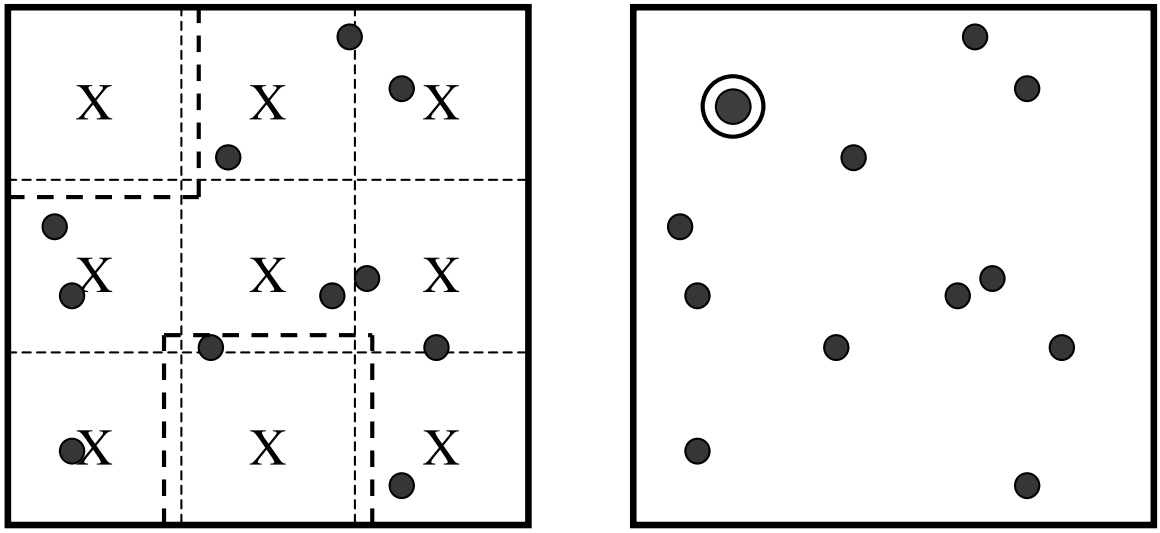

Figure 8: ALPM: Creation step for $N_{\text{part}}^{\text{elt,min}} = 3 \times 3$. The crosses denote the Reference Locations (RL), while the black circles are the Lagrangian particles present in the element. Since no particle is found close enough to the upper-left RL, a new particle is created there.

5.2 Initialization of the configuration state

Once a new particle is created at time t_n in an element, its configuration state must be properly initialized in order to allow for the solution between t_n and t_{n+1} of the constitutive or stochastic differential equation along the particle's path (Fig. 9). The initialization step is again performed in an element-by-element fashion. Ideally, one would wish to somehow preserve the polymer

stress field $\boldsymbol{\tau}_p(t_n)$ computed in the element at the previous time step. Within an isotropic term, the polymer stress (8) is proportional to $\langle \boldsymbol{Q}\boldsymbol{F}^c(\boldsymbol{Q})\rangle$. On the basis of the Lagrangian particles present in the element at time t_n, one can compute the linear least-squares polynomial that fits the available $\langle \boldsymbol{Q}\boldsymbol{F}^c(\boldsymbol{Q})\rangle$ Lagrangian data. The polymer stress $\langle \boldsymbol{Q}\boldsymbol{F}^c(\boldsymbol{Q})\rangle^{(\text{new part})}$ at the new particle's location is then obtained by interpolation. The remaining task is to compute the configuration state of the new particle that gives the polymer stress $\langle \boldsymbol{Q}\boldsymbol{F}^c(\boldsymbol{Q})\rangle^{(\text{new part})}$. For the FENE-P fluid, the configuration state is given by the second moment $\boldsymbol{A} = \langle \boldsymbol{Q}\boldsymbol{Q}\rangle$. In view of (10), we have

$$\langle \boldsymbol{Q}\boldsymbol{F}^c(\boldsymbol{Q})\rangle^{(\text{new part})} = \frac{H\boldsymbol{A}}{1 - \text{tr}(\boldsymbol{A})/Q_0^2}, \tag{22}$$

which is readily inverted to initialize the configuration $\boldsymbol{A}$ of the new particle at time t_n.

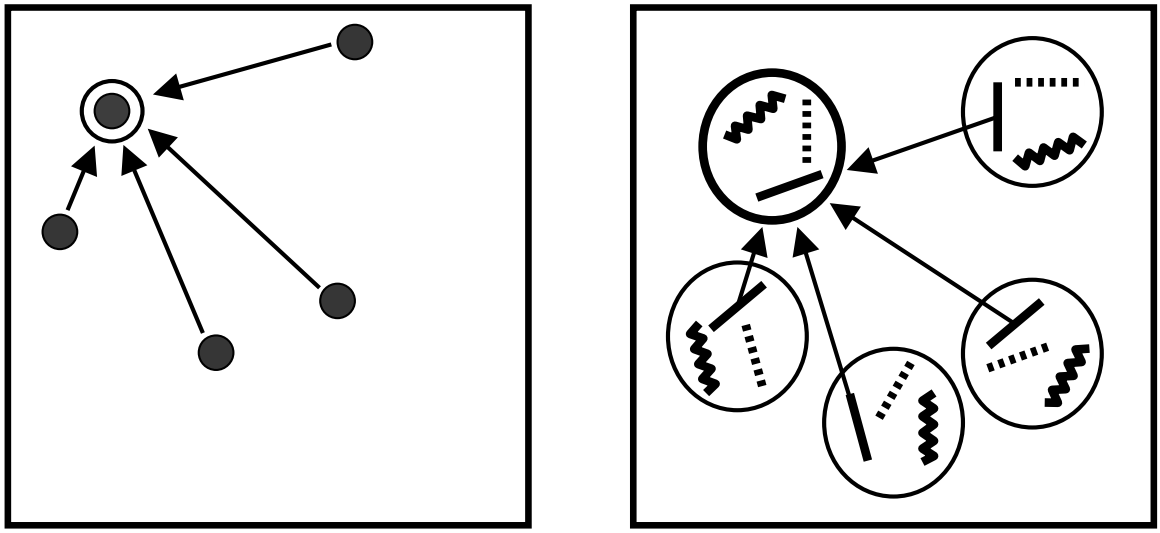

Figure 9: ALPM: Initialization step for the new particle created at the upper-left corner of the element. FENE-P fluid (left): the arrows illustrate the least-squares process used to compute $\langle \boldsymbol{Q}\boldsymbol{F}^c(\boldsymbol{Q})\rangle$ at the new particle using existing Lagrangian data. FENE fluid (right): the least-squares process is performed using individual dumbbell data. Each particle carries three dumbbells, for the sake of illustration. Dumbbells of the same "type" are statistically correlated.

For the FENE dumbbell kinetic theory, the configuration state is given by the set of connector vectors $\{\boldsymbol{Q}^{(i)}, i = 1, 2, \ldots, N_d\}$ of the dumbbells carried

by the particle. In view of (6), we have

$$\langle \boldsymbol{Q}\boldsymbol{F}^c(\boldsymbol{Q})\rangle^{(\text{new part})} = \langle \frac{H\boldsymbol{Q}\boldsymbol{Q}}{1-\text{tr}(\boldsymbol{Q}\boldsymbol{Q})/Q_0^2}\rangle \sim \frac{H}{N_d}\sum_{i=1}^{N_d}\frac{\boldsymbol{Q}^{(i)}\boldsymbol{Q}^{(i)}}{1-\text{tr}(\boldsymbol{Q}^{(i)}\boldsymbol{Q}^{(i)})/Q_0^2}. \tag{23}$$

The difficulty with (23) is clear: it is not possible to compute the set $\{\boldsymbol{Q}^{(i)}\}$ by direct inversion of (23), as we did for the FENE-P configuration tensor $\boldsymbol{A}$. Another approach is thus called for. We propose to initialize the connector vector of dumbbell $\#i$ by means of a linear least-squares approximation based on the $\boldsymbol{Q}^{(i)}$'s of the corresponding i^{th} dumbbell carried by the particles present in the element at time t_n (Fig. 9). Obviously, this procedure can only be used with *correlated* ensembles of dumbbells.

5.3 Destruction of Lagrangian particles

The destruction step allows ALPM to enforce a maximum of $N_{\text{part}}^{\text{elt,max}}$ particles in each element (Fig. 10). The element-by-element destruction loops goes as follows, as long as the number of particles is larger than $N_{\text{part}}^{\text{elt,max}}$: (i) Find the two particles LP^1 and LP^2 that are closest to each other, (ii) Create a new particle LP^{new} in between LP^1 and LP^2, (iii) Initialize the configuration state of LP^{new}, and (iv) Remove LP^1 and LP^2. The initialization step (iii) is a simple arithmetic mean of either the configuration tensor $\boldsymbol{A}$ (FENE-P model), or the i^{th} dumbbell connector vector $\boldsymbol{Q}^{(i)}, i = 1, 2, \ldots, N_d$ (FENE fluid).

6 ALPM applied to the large-eccentricity journal bearing problem

6.1 FENE-P fluid

Figure 11 shows the large-eccentricity results obtained with ALPM and the FENE-P fluid. The mesh is that of Fig. 2, and the time steps are $\Delta t_{\text{cons}} = 10^{-2}$ and $\Delta t_{\text{track}} = \Delta t_{\text{const}} = 10^{-3}$. This particular simulation ensures that the number of particles in each element is always in the interval $[N_{\text{part}}^{\text{elt,min}}, N_{\text{part}}^{\text{elt,max}}] = [9, 20]$. Clearly, ALPM produces satisfactory results even with such a small number of particles. Not surprisingly, Fig. 11 shows that ALPM has created new particles near the moving cylinder only.

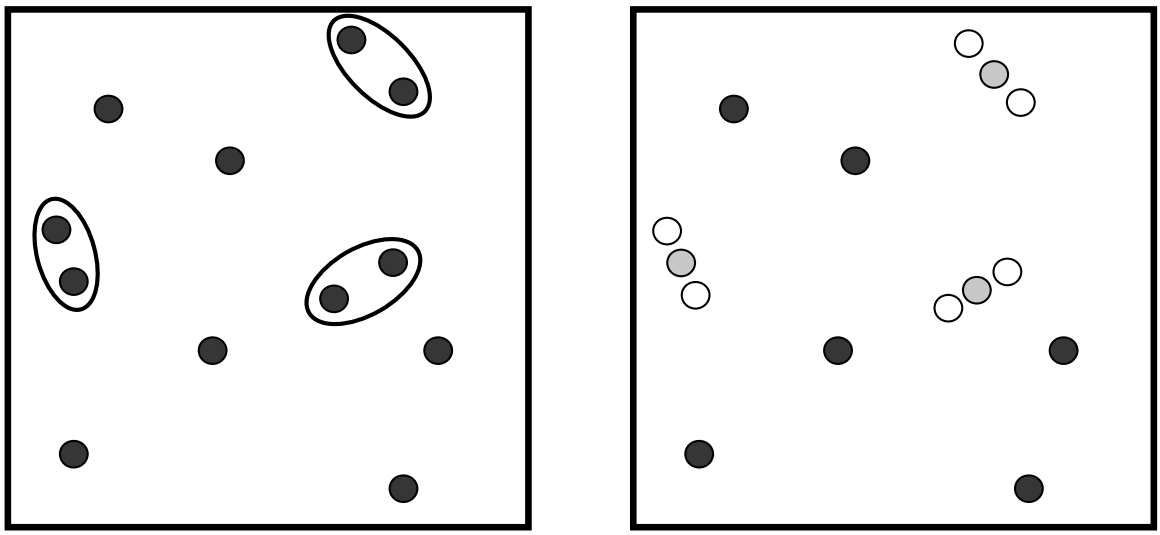

Figure 10: ALPM: Destruction step for $N_{\text{part}}^{\text{elt,max}} = 9$. Left: Three particle pairs (LP^1, LP^2) are identified. Right: Three new particles are created in between the LP^1 and LP^2 particles; the latter are removed.

Convergence of the ALPM results to the LPM reference solution (obtained with $N_{\text{part}}^{\text{elt}} = 2025$) is illustrated in Fig. 12. Here we show the temporal evolution of the polymer stress computed by ALPM with $[N_{\text{part}}^{\text{elt,min}}, N_{\text{part}}^{\text{elt,max}}] = [9, 20]$, $[25, 50]$, and $[121, 150]$ respectively, all other numerical parameters being kept unchanged. The polymer stress transient computed with ALPM is quite smooth; numerical oscillations somewhat affect the steady-state, but the amplitude of these spurious oscillations decreases when the number of particles increases.

Contour lines of the velocity v_y and the normal stress difference $\tau_{yy} - \tau_{xx}$ are shown in Fig. 13. Here we give the results at time $t = 10$ of two ALPM simulations for the FENE-P fluid, with $[N_{\text{part}}^{\text{elt,min}}, N_{\text{part}}^{\text{elt,max}}] = [9, 20]$ and $[121, 150]$, respectively. The results are in good agreement. One notes also the satisfactory smoothness of the polymer stress field.

6.2 FENE fluid

Figure 14 shows the large-eccentricity results obtained with ALPM and the FENE dumbbell kinetic theory. The mesh is again that of Fig. 2, and the time steps are $\Delta t_{\text{cons}} = \Delta t_{\text{track}} = \Delta t_{\text{stoch}} = 10^{-2}$. Two simulations

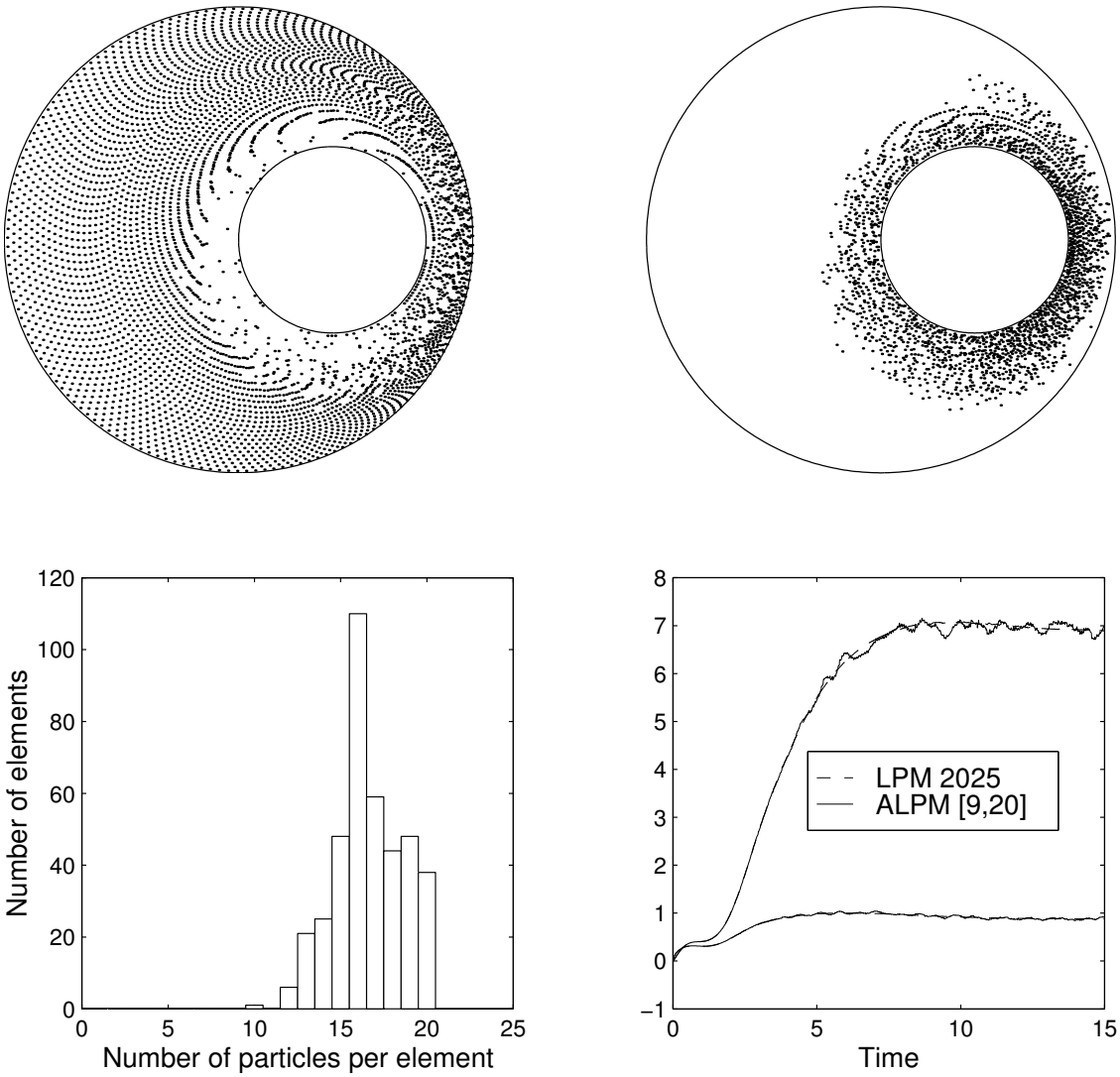

Figure 11: ALPM simulation for the FENE-P fluid with $[N_{\rm part}^{\rm elt,min}, N_{\rm part}^{\rm elt,max}] = [9, 20]$. Upper-left: spatial locations at time $t = 10$ of particles that were present in the initial ensemble of particles at $t = 0$. Upper-right: spatial locations at time $t = 10$ of particles created during the course of the simulation. Lower-left: statistical distribution of particles at time $t = 10$. Lower-right: temporal evolution of the polymer stress in the region of thinnest gap (see Fig. 2); the LPM 2025 reference solution is also shown.

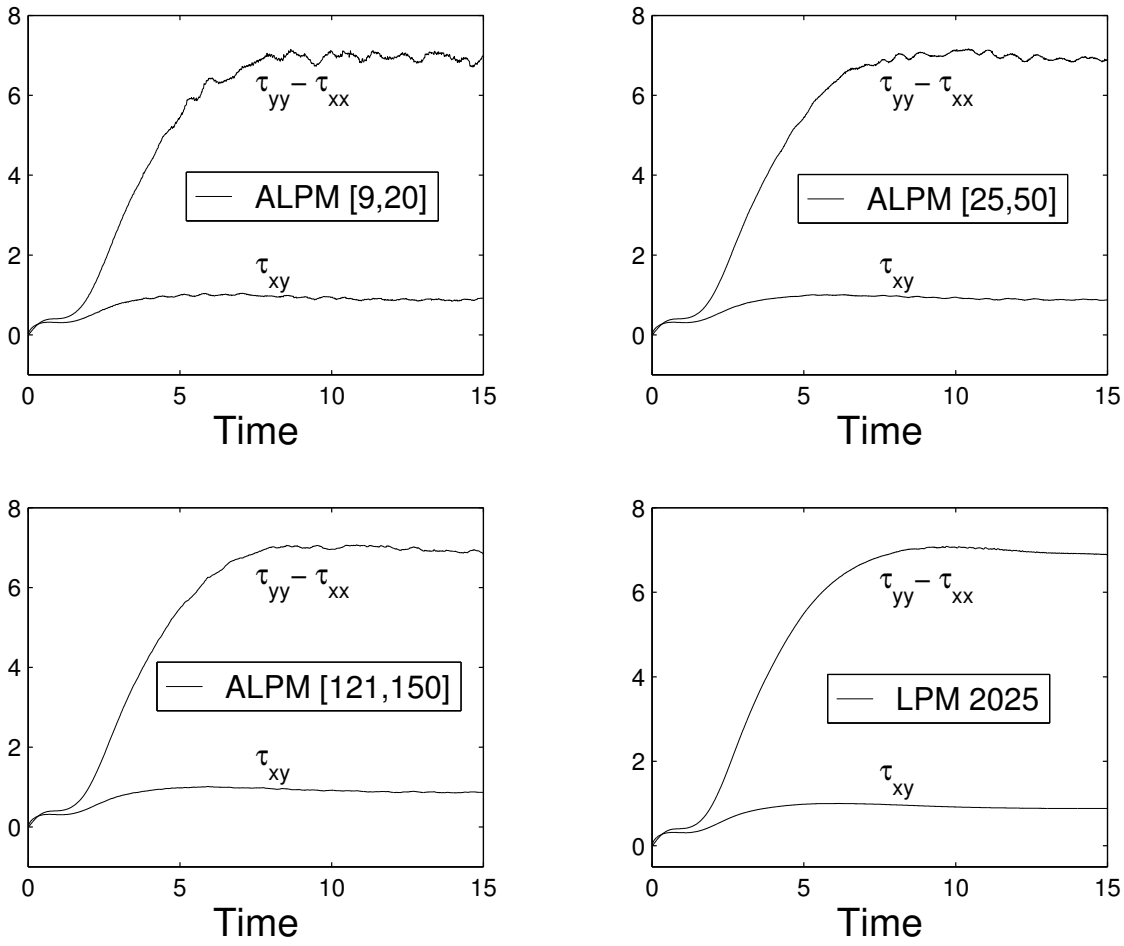

Figure 12: ALPM simulation for the FENE-P fluid using various values of $[N_{\text{part}}^{\text{elt,min}}, N_{\text{part}}^{\text{elt,max}}]$. Temporal evolution of the polymer stress in the region of thinnest gap (see Fig. 2). Convergence to the LPM 2025 reference solution is observed.

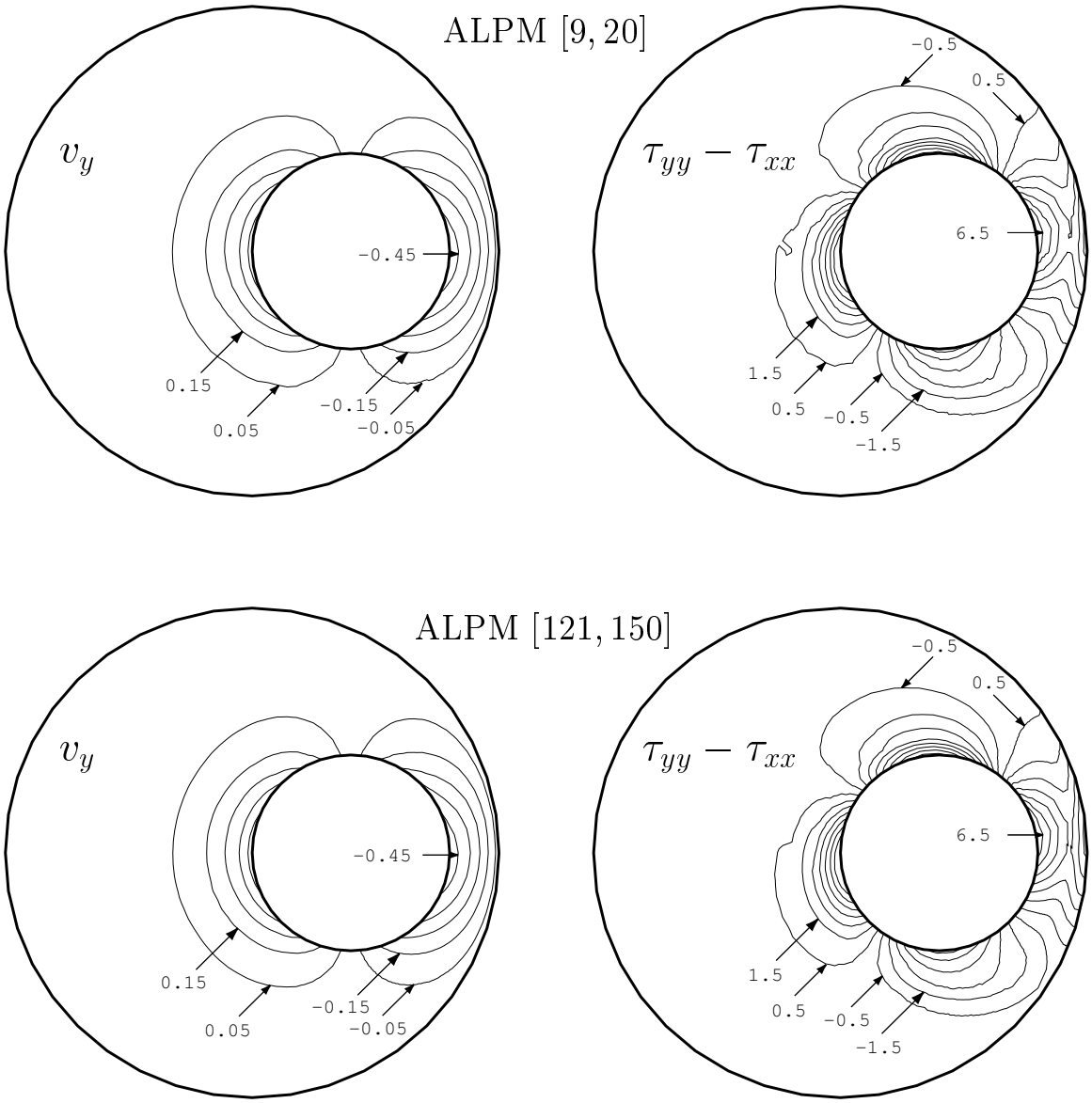

Figure 13: ALPM simulation for the FENE-P fluid. Contour lines of velocity and polymer stress at time $t = 10$ obtained with $[N_{\text{part}}^{\text{elt,min}}, N_{\text{part}}^{\text{elt,max}}] = [9, 20]$ and $[121, 150]$. A constant increment of 0.1 and 1.0 is used for the velocity and stress, respectively.

are illustrated, with $[N_{\rm part}^{\rm elt,min}, N_{\rm part}^{\rm elt,max}] = [9, 20]$ and $[25, 50]$, and $N_d = 5000$ and 3000 dumbbells in each particle, respectively. The smoothness of these micro-macro results is noteworthy. The FENE-P solution is also shown for comparison purposes. In this particular flow problem, the velocity field is found to be unaffected by the Peterlin closure approximation (at least for the case $De = 1$ studied here). The FENE and FENE-P polymer stresses, however, are indeed very different.

The temporal evolution of the velocity and polymer stress fields is illustrated in Figs. 15 and 16. Here, we plot contour lines of the velocity v_y and the normal stress difference $\tau_{yy} - \tau_{xx}$ at selected values of time, for $[N_{\rm part}^{\rm elt,min}, N_{\rm part}^{\rm elt,max}] = [25, 50]$ and $N_d = 3000$.

A velocity overshoot is predicted at $t = 1$ (cfr Fig. 14) in the region of thin gap. The fluid is also found to move quite rapidly during the transient phase ($t = 2$) in the region of large gap.

On the whole, the computed velocity and stress fields are quite smooth during the transient phase. As observed already with the FENE-P model, spurious oscillations somewhat perturb the steady-state solution. Their amplitude is not dramatic, however.

The micro-macro ALPM simulations for the FENE fluid provide a wealth of information regarding the flow-induced evolution of the polymer configuration. For example, we show in Fig. 17 how the flow has distorted the initial distribution of dumbbell length near the wall, in the region of thinnest gap.

7 Discussion and conclusions

We have demonstrated in the present paper the ability of ALPM of producing accurate numerical results for the time-dependent flow of a viscoelastic fluid between highly-eccentric cylinders, using either a macroscopic constitutive equation of the differential type (FENE-P model) or a kinetic theory model (FENE dumbbells). ALPM is clearly a step forward relative to its parent LPM, which was used successfully in [14] for solving the small-eccentricity journal bearing problem.

Table 2 compares LPM and ALPM in terms of the computer resources (CPU time and central memory capacity) needed to produce the results of Sections 4 and 6. The FENE-P simulations were performed on a single DEC Alpha processor, while the FENE calculations were run on a farm of 10 DEC

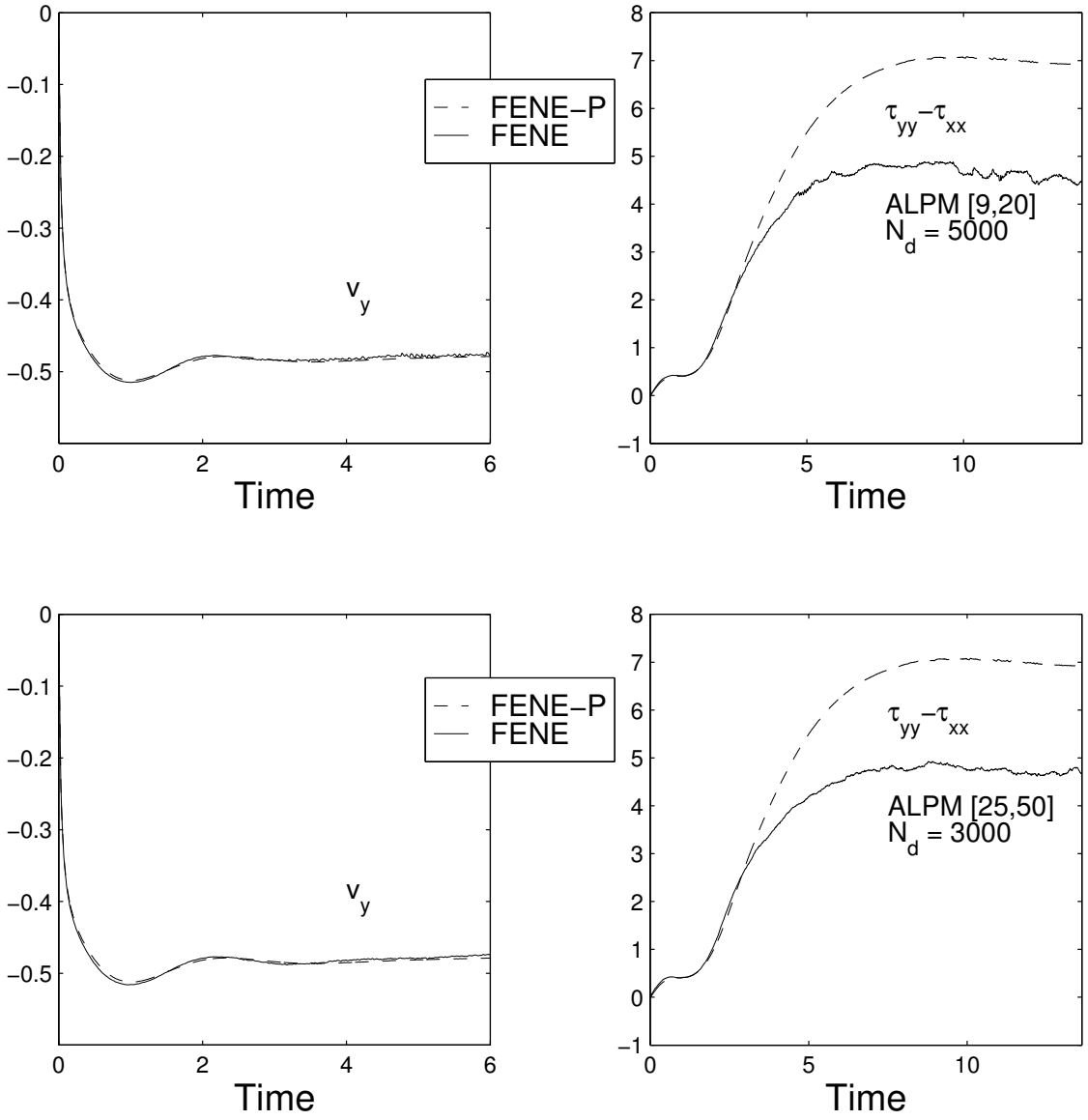

Figure 14: ALPM simulation for the FENE fluid. Temporal evolution of velocity and polymer stress in the region of thinnest gap (see Fig. 2). Results for $[N_{\rm part}^{\rm elt,min}, N_{\rm part}^{\rm elt,max}] = [9, 20]$ and $[25, 50]$ with a number N_d of dumbbells in each particle equal to 5000 and 3000, respectively. The FENE-P results are shown for comparison purposes.

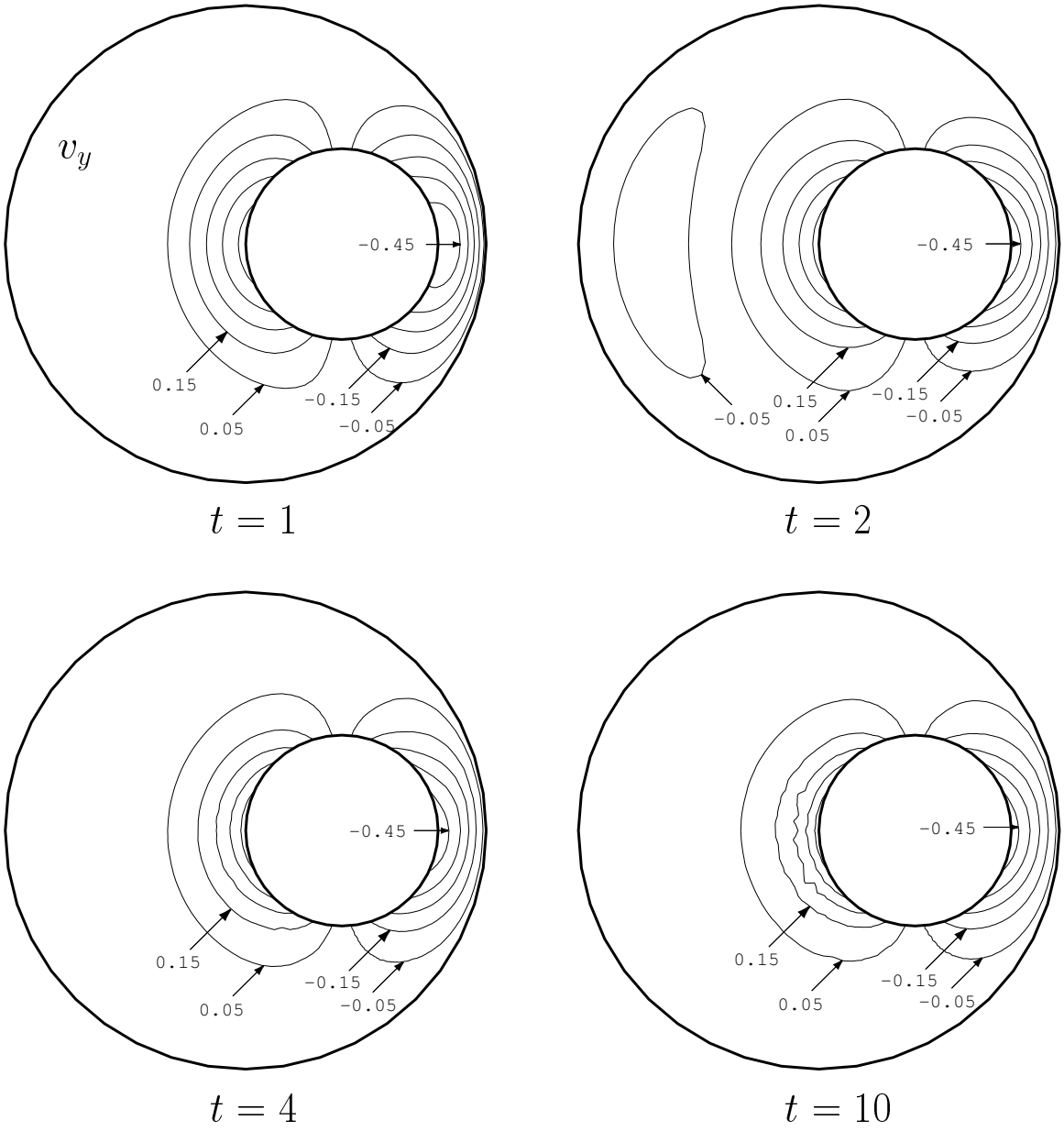

Figure 15: ALPM simulation for the FENE fluid with $[N_{\text{part}}^{\text{elt,min}}, N_{\text{part}}^{\text{elt,max}}] = [25, 50]$ and $N_d = 3000$. Temporal evolution of the contour lines of the v_y velocity component. A constant increment of 0.1 is used for each snapshot.

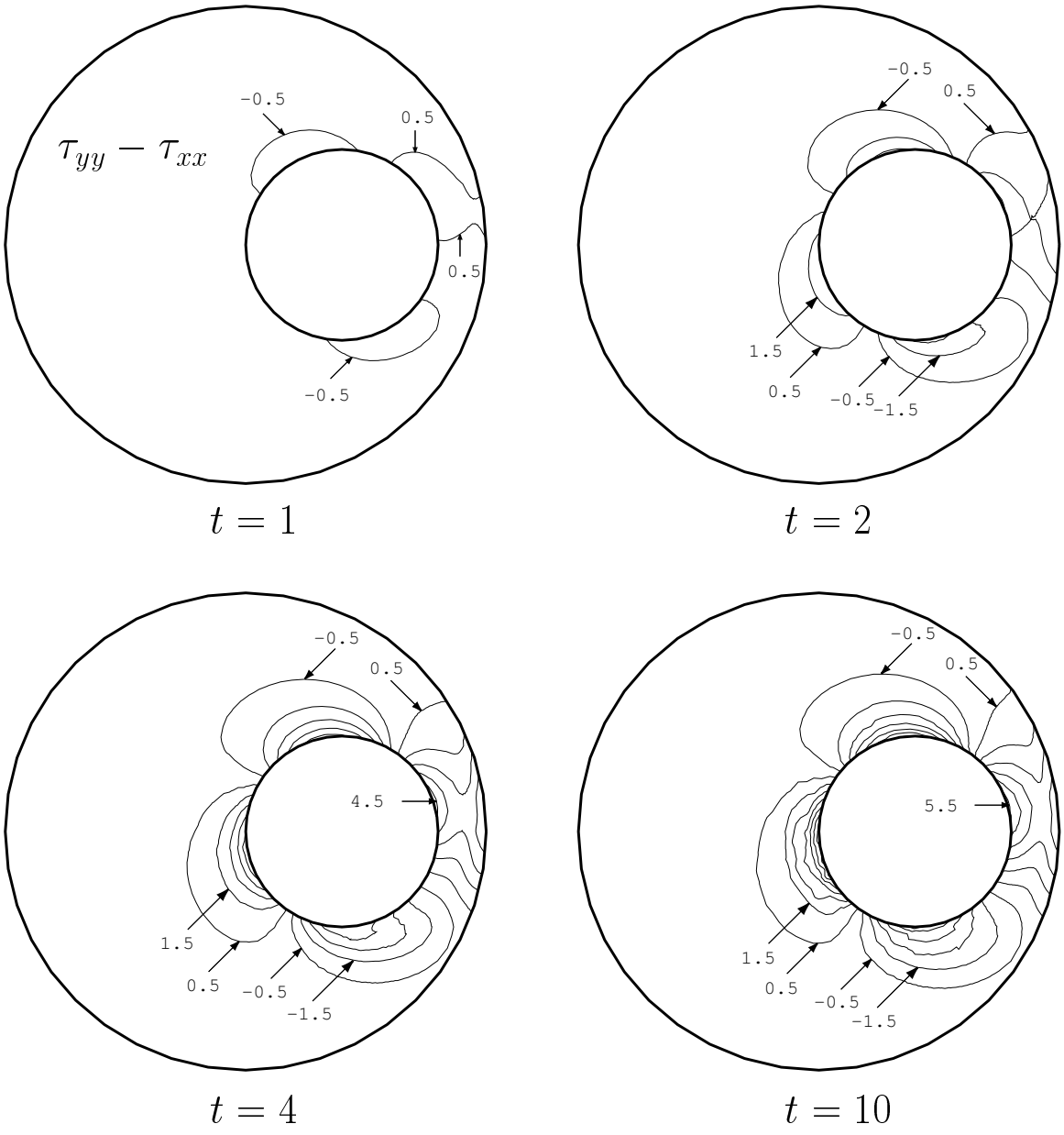

Figure 16: ALPM simulation for the FENE fluid with $[N_{\text{part}}^{\text{elt,min}}, N_{\text{part}}^{\text{elt,max}}] = [25, 50]$ and $N_d = 3000$. Temporal evolution of the contour lines of the first normal stress difference $\tau_{yy} - \tau_{xx}$. A constant increment of 1.0 is used for each snapshot.

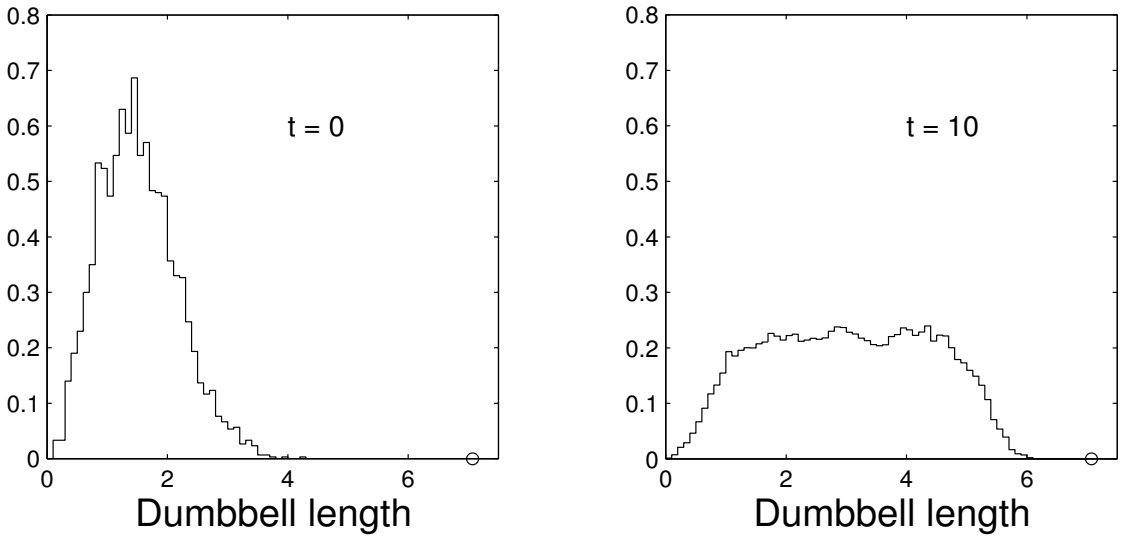

Figure 17: ALPM simulation for the FENE fluid with $[N_{\text{part}}^{\text{elt,min}}, N_{\text{part}}^{\text{elt,max}}] = [9, 20]$ and $N_d = 5000$. Distribution of dumbbell length at time $t = 0$ and $t = 10$ computed near the wall in the region of thinnest gap. The histograms are drawn using the Lagrangian data available in the two finite elements containing the point ($\bullet$) of Figure 2. Dumbbell length is made dimensionless with $\sqrt{kT/H}$. The circle on the horizontal axis marks the upper limit $\sqrt{b}$.

Alpha processors connected through a 100 MHz switch. Details on the MPI-based parallel implementation of ALPM are given elsewhere [27]. Briefly, we distribute the N_d dumbbells carried by each Lagrangian particle to the P available processors, and compute their configuration in parallel. A communication phase is needed to assemble in each processor the contributions of the P processors to the polymer stress. The remaining ALPM calculations, which are much less expensive than the stochastic simulation step, are then performed redundantly by all processors in order to avoid further communication overheads.

One observes in Table 2 that the LPM timing and memory data follow a linear behaviour of the form $a+bN_{\text{part}}$, where the constant a is the cost of the Eulerian macroscopic solution of the conservation equations (Fig. 1). The CPU time quoted in Table 2 is per macroscopic time step. So, the total run time of the LPM 2025 FENE-P simulation of Fig. 12, over the time interval $[t_0, t_f] = [0, 15]$, amounts to about 54.2 hours. The computer resources used by the corresponding ALPM $[121, 150]$ run are about ten times less. This is of great significance for the micro-macro FENE simulations, which are by nature quite demanding in computer memory. In fact, the ALPM $[25, 50]$ simulation for the FENE fluid (Fig. 14) used a total of 1.2 GB of core memory; the corresponding LPM 2025 FENE simulation whould have required about 10 GB, which is not feasible on standard hardware.

The basic adaptive algorithm proposed in Section 5 is amenable to further developments in a number of directions. In particular, criteria remain to be developed for selecting the interval $[N_{\text{part}}^{\text{elt,min}}, N_{\text{part}}^{\text{elt,max}}]$ that governs the creation and destruction steps. Also, the initialization of the configuration state in the micro-macro ALPM simulations deserves further investigations. Other issues may arise as we gain more experience with ALPM in a variety of flow problems. Nevertheless, the results reported in this paper do show the feasibility and value of ALPM for solving non-trivial viscoelastic flow problems with a constitutive equation or a kinetic theory model for the polymer dynamics.

Acknowledgments

This work is supported by the ARC 97/02-210 project, Communauté Française de Belgique, and the BRITE/EURAM project MPFLOW CT96-0145. The work of V. Legat is supported by the Belgian *Fonds National de la*

Recherche Scientifique (FNRS).

References

[1] R.I. Tanner and K. Walters. *Rheology: an Historical Perspective*. Elsevier, 1998.

[2] M.J. Crochet, A.R. Davies, and K. Walters. *Numerical Simulation of Non-Newtonian Flow*. Elsevier, 1984.

[3] M.J. Crochet. Simulation of viscoelastic flow. Rubber Chemistry and Technology. *Amer. Chem. Soc.*, 62:426–455, 1989.

[4] R. Keunings. Simulation of viscoelastic fluid flow. In C. L. Tucker III, editor, *Fundamentals of Computer Modeling for Polymer Processing*, pages 402–470. Carl Hanser Verlag, 1989.

[5] R. Keunings and P. Halin. Macroscopic and mesoscale approaches to the computer simulation of viscoelastic flows. In J.R.A. Pearson M.J. Adams, R.A. Mashelkar and A.R. Rennie, editors, *Dynamics of Complex Fluids*, pages 88–105. Imperial College Press - The Royal Society, 1998.

[6] F.P.T Baaijens. Mixed finite element methods for viscoelastic flow analysis: a review. *J. Non-Newtonian Fluid Mech.*, in press, 1998.

[7] H.C. Öttinger and M. Laso. "Smart" polymers in finite-element calculations. In P. Moldenaers and R. Keunings, editors, *Proceedings of the XIth International Congress on Rheology*, pages 286–288. Elsevier, Amsterdam, 1992.

[8] M. Laso and H.C. Öttinger. Calculation of viscoelastic flow using molecular models: the CONNFFESSIT approach. *J. Non-Newtonian Fluid Mech.*, 47:1–20, 1993.

[9] K. Feigl, M. Laso, and H.C. Öttinger. The CONNFFESSIT approach for solving a two-dimensional viscoelastic fluid problem. *Macromolecules*, 28:3261–3274, 1995.

[10] C.C. Hua and J.D. Schieber. Application of kinetic theory models in spatiotemporal flows for polymer solutions, liquid crystals and polymer melts using the CONNFFESSIT approach. *Chem. Eng. Sci.*, 51:1473–1485, 1996.

[11] M. Laso, M. Picasso, and H.C. Öttinger. 2-D time-dependent viscoelastic flow calculations using CONNFFESSIT. *AIChE Journal*, 43:877–892, 1997.

[12] M.A. Hulsen, A.P.G. van Heel, and B.H.A.A. van den Brule. Simulation of viscoelastic flows using Brownian configuration fields. *J. Non-Newtonian Fluid Mech.*, 70:79–101, 1997.

[13] T.W. Bell, G.H. Nyland, J.J. de Pablo, and M.D. Graham. Combined Brownian dynamics and spectral simulation of the recovery of polymeric fluids after shear flow. *Macromolecules*, 30:1806–1812, 1997.

[14] P. Halin, R. Keunings, and V. Legat. The Lagrangian particle method for macroscopic and micro-macro viscoelastic flow computations. *J. Non-Newtonian Fluid Mech.*, in press, 1998.

[15] R.B. Bird, C.F. Curtiss, R.C. Armstrong, and O. Hassager. *Dynamics of Polymeric Liquids, Vol.2, Kinetic theory.* Wiley-Interscience, New York, 2nd edition 1987.

[16] M.J. Crochet and R. Keunings. On numerical die swell calculation. *J. Non-Newtonian Fluid Mech.*, 10:85–94, 1982.

[17] D.W. Bousfield, R. Keunings, G. Marrucci, and M.M. Denn. Nonlinear analysis of the surface tension driven breakup of viscoelastic filaments. *J. Non-Newtonian Fluid Mech.*, 21:79–97, 1986.

[18] R. Keunings. An algorithm for the simulation of transient viscoelastic flows with free surfaces. *Computational Physics*, 62:199–220, 1986.

[19] S. Musarra and R. Keunings. Co-current axisymmetric flow in complex geometries: Numerical simulation. *J. Non-Newtonian Fluid Mech.*, 32:253–268, 1989.

[20] M.R.J. Verhoef, B.H.A.A. van den Brule, and M.A. Hulsen. On the modelling of a PIB/PB Boger fluid in extensional flow. *J. Non-Newtonian Fluid Mech.*, in press, 1998.

[21] G. Lielens, P. Halin, I. Jaumain, R. Keunings, and V. Legat. New closure approximations for the kinetic theory of finitely extensible dumbbells. *J. Non-Newtonian Fluid Mech.*, 76:249–279, 1998.

[22] R. Sizaire, G. Lielens, I. Jaumain, R. Keunings, and V. Legat. On the hysteretic behaviour of dilute polymer solutions in relaxation following extensional flow. *J. Non-Newtonian Fluid Mech.*, in press, 1998.

[23] M. Herrchen and H.C. Öttinger. A detailed comparison of various FENE dumbbell models. *J. Non-Newtonian Fluid Mech.*, 68:17–42, 1997.

[24] R. Keunings. On the Peterlin approximation for finitely extensible dumbbells. *J. Non-Newtonian Fluid Mech.*, 68:85–100, 1997.

[25] R.B. Bird, R.C. Armstrong, and O. Hassager. *Dynamics of Polymeric Liquids, Vol.1, Fluid mechanics.* Wiley-Interscience, New York, 2nd edition 1987.

[26] H.C. Öttinger. *Stochastic Processes in Polymeric Fluids: Tools and Examples for Developing Simulation Algorithms.* Springer, Berlin, 1996.

[27] X. Gallez. PhD thesis, Université catholique de Louvain, Belgium, in preparation.

Model	Method	CPU time (s)	Memory (MB)
FENE-P (1 proc.)	LPM 9	3.33	7
	LPM 25	4.15	8
	LPM 100	9.10	17
	LPM 256	18.74	35
	LPM 2025	130.04	235
FENE-P (1 proc.)	ALPM $[9, 20]$	3.61	8
	ALPM $[25, 50]$	5.52	12
	ALPM $[121, 150]$	15.18	30
FENE (10 proc.)	ALPM $[9, 20]$	9.04	10×60
	ALPM $[25, 50]$	31.97	10×120

Table 2: Computer resources for the LPM and ALPM simulations reported in the present paper. The CPU time is quoted per macroscopic time step ($\Delta t_{\text{cons}} = 10^{-2}$). All simulations used the 10×40 mesh of Fig. 2. The FENE-P results were obtained with a single DEC Alpha 533MHz processor, while the FENE simulations used 10 processors in parallel.